

# Spin-dependent photovoltage in graphene/MoS<sub>2</sub>-based field-effect transistors

K. Dinar<sup>1</sup>, J. Delgado-Notario<sup>2</sup>, C. Bray<sup>1</sup>, K. Maussang<sup>3</sup>, E. Perez-Martin<sup>3</sup>, B. Benhamou-Bui<sup>1</sup>, C. Consejo<sup>1</sup>, S. Ruffenach<sup>1</sup>, S. S. Krishtopenko<sup>1</sup>, L. Bonnet<sup>1</sup>, M. Paillet<sup>1</sup>, J. Torres<sup>1</sup>, Y. M. Meziani<sup>2</sup>, I. Rozhansky<sup>4</sup>, B. Jouault<sup>1</sup>, S. Nanot<sup>1</sup>, F. Teppe<sup>1\*</sup>

<sup>1</sup> L2C (UMR 5221), Université de Montpellier, CNRS, Montpellier, France

<sup>2</sup> Nanotechnology Group, USAL-Nanolab, Universidad de Salamanca, Salamanca 37008, Spain

<sup>3</sup> IES (UMR 5214), Université de Montpellier, CNRS, Montpellier, France

<sup>4</sup> National Graphene Institute, University of Manchester, Manchester M13 9PL, United Kingdom

\* [frederic.teppe@umontpellier.fr](mailto:frederic.teppe@umontpellier.fr)

**It has recently been shown that Terahertz sensors can effectively detect the spin resonances of Dirac fermions in graphene. The associated photovoltaic measurement technique allows for the investigation of the intrinsic spin-orbit coupling in graphene as well as its topological properties from microwave to Terahertz frequencies. In this work, using graphene/MoS<sub>2</sub>-based Field-Effect Transistors, we observed a magnetic resonance photovoltage signal in the Gigahertz range that is independent on the gate bias. The dispersion of the associated spin-flip transitions remains intriguingly unaffected by the MoS<sub>2</sub> layer. In parallel, the spin-related signal consistently appears as a drop in photovoltage, regardless of the signal's polarity or origin, whether it is due to plasma wave rectification or thermoelectric effects. This behavior is interpreted as a decrease in the system's spin polarization due to spin-dependent recombination or scattering of photocarriers. Understanding the various photovoltaic signals in highly sensitive Gigahertz/Terahertz sensors paves the way for exploring spin-dependent mechanisms in two-dimensional quantum materials, influenced by proximity effects such as spin-orbit coupling, topology, and magnetism.**

---

## Introduction

Over the years, numerous broadband and resonant Terahertz (THz) detectors have been developed, using a wide range of materials and diverse physical mechanisms. These include the Ratchet effect in asymmetric uni- or bi-dimensional structures [<sup>1,2,3</sup>], thermal effects such as bolometric [<sup>4,5</sup>] or thermoelectric responses like the Seebeck effect [<sup>6,7</sup>], and Schottky rectification [<sup>8,9,10</sup>]. Among the different approaches, one particularly notable method was proposed three decades ago by M. Dyakonov

and M. Shur [11, 12]. They suggested that field-effect transistors (FETs) could detect Terahertz (THz) electromagnetic radiation through rectification of plasmonic oscillations in the two-dimensional (2D) electron gas within the transistor's channel. Since that time, many materials have been explored to design and optimize these broadband or resonant THz detectors [13], including silicon [14, 15], GaAs [16, 17, 18], InGaAs [19, 20], GaN [21], HgCdTe [22, 23, 24], as well as graphene [25, 26, 27].

These different THz detectors enable the study of numerous physical properties of the materials used, such as crystalline or structural symmetries [28], non-linear carrier dynamics [29, 30], plasmons and magneto-plasmons [31, 32], and Landau level transitions [33]. Interestingly, they can also serve as efficient probes of the high-frequency spin properties of electrons under strong magnetic fields. Based on the ratchet effect in an interdigitated asymmetric top gate device in the presence of a magnetic field, the influence of temperature on different spin and valley splittings in single and bilayer graphene was recently studied [34]. Three electronic spin resonances (ESRs) were indeed identified over a frequency range of 45 GHz to 220 GHz. However, despite a high THz sensitivity, the amplitude of the electron spin resonance (ESR) signal remained relatively weak, i.e., comparable to the signal obtained with the classical electrically detected ESR (EDESER) transport-based technique [57, 58, 59], and the precise origin of this rectification signal was still unclear. To further develop this novel sub-THz photovoltaic ESR technique (PV-ESR), it is therefore necessary to better understand the origin of this ESR signal and to optimize the photovoltaic/photoconductive ESR devices.

In this work, we explore the origin of the ESR signal measured by magneto-photoconductivity in a plasma wave detector based on a monolayer graphene/MoS<sub>2</sub> FET. The underlying idea of this structure is to enhance the spin-orbit coupling in the graphene layer through proximity effects with the MoS<sub>2</sub> layer as predicted theoretically in [35]. We clearly observe three different contributions to this photovoltaic signal. A part of the signal depends on the gate voltage and is related to the non-resonant rectification of the incident radiation by the overdamped plasma waves in the channel. The second contribution to the signal, that takes the form of an offset in a particular measurement configuration, is interpreted as due to a thermoelectric effect at the metal-graphene interface with a different temperature change induced at the source and drain contacts of the channel. The last part of the signal appears in the presence of a magnetic field and consists in pronounced electron spin resonances, as already observed in [34]. Our experimental results clearly highlight the fact that the PV-ESR signal consistently appears as a drop in photovoltage. This phenomenon is interpreted as a decrease in the system's spin polarization due to spin-charge conversion, improving our understanding of the origin of the PV-ESR signal. Furthermore, four electron spin resonances are clearly observed and studied as a function of the incident frequency. Interestingly, despite the presence of the MoS<sub>2</sub> layer, the observed g-factor and zero field splittings (ZFS) are similar to those observed in pristine monolayer graphene samples that are either CVD-grown or embedded between h-BN. The PV-ESR method thus provides an opportunity to investigate spin-

dependent mechanisms in two-dimensional quantum materials influenced by proximity effects, directly within nanoscale FETs. This approach eliminates the need for a cavity or direct contact with the excitation source and operates across a broad frequency range, from a few GHz to several THz.

### Sample and characterization

The plasma wave FET detector studied in our work was fabricated from monolayer graphene and a monolayer of MoS<sub>2</sub>. The monolayer graphene and MoS<sub>2</sub> layers were encapsulated between two layers of hexagonal boron nitride (hBN) using standard dry transfer techniques then deposited on a Si substrate with a 300 nm thick SiO<sub>2</sub> layer. The resulting device was patterned in a FET geometry with a channel length of 2 μm and a width of 14 μm. A schematic view of the fabricated device is shown in Figure 1(a). The two contacts were fabricated using electron beam lithography (EBL), followed by metallization (Cr/Au, 5 nm/45 nm) and standard liftoff processes. The device also includes a metallic 500 nm-long top gate connected by one arm to a bow-tie antenna of radius 250 μm (Fig.1(c)). The second part of the bow-tie antenna is connected to one of the two contacts, which we label as the “source” contact in the following. We label the remaining contact as the ‘drain’. This geometry is typical for plasma wave THz sensors and is known as the Dyakonov–Shur scheme [36]. It allows non-resonant detection of incident waves over a very broad spectral range. More detailed information on the sample fabrication can be found in [37].

Although Raman spectroscopy confirms the presence of a graphene monolayer and indicates a good coupling between the graphene and the MoS<sub>2</sub> sheets (see Supplementary Materials, Figure SM1), the electrical characterization does not show any clear contribution of the MoS<sub>2</sub> layer (neither as a gate-sensitive parallel conduction channel, nor *via* proximity effect). Moreover, the Si/SiO<sub>2</sub> substrate which was initially intended to be used as a back gate exhibited a non-negligible leakage current. However, the device resistance could still be measured reliably as a function of source-drain and source-top gate voltages (see Supplementary Materials, Figure SM2).

The signal consists of a voltage drop between the source and drain contacts which originates from the rectification of the THz wave by the overdamped plasma waves. In the following we label  $\Delta U_{SD}$  the voltage drop  $U_S - U_D$  between the source and drain contacts when the “drain” is grounded (see Fig. 1a). By contrast, we label  $\Delta U_{DS}$  the voltage drop between the drain and source contact when the “source” is grounded (see Fig.1b). A clear asymmetry between the source and drain is highlighted by the resistances  $\Delta U_{DS}/I$  and  $\Delta U_{SD}/I$ , where  $I$  is the current injected into the device. These two-probe resistances are indeed different, see Fig. SM2a. As the source-drain characteristics remain linear, see Fig. SM2b, the asymmetry cannot be explained by the presence of Schottky barriers. This difference could be due to irregularities in the metal contacts or unintentional charging effects due to the presence of MoS<sub>2</sub> and the SiO<sub>2</sub>/Si back gate beneath the graphene layer. Since the signal from over-damped plasma wave

rectification clearly manifests itself in transconductance [38], Figure 1(d) represents the transconductances on both sides of the channel. These curves already suggest a different photovoltage depending on which contact is grounded. Given the low current variation on the source side when crossing the charge neutrality point (CNP), the photovoltage is expected to be weak. On the drain side, however, the photovoltage from the damped plasma waves is expected to be stronger. These predictions agree well with the photovoltage measurements shown in Figures 1(e) and 1(f).

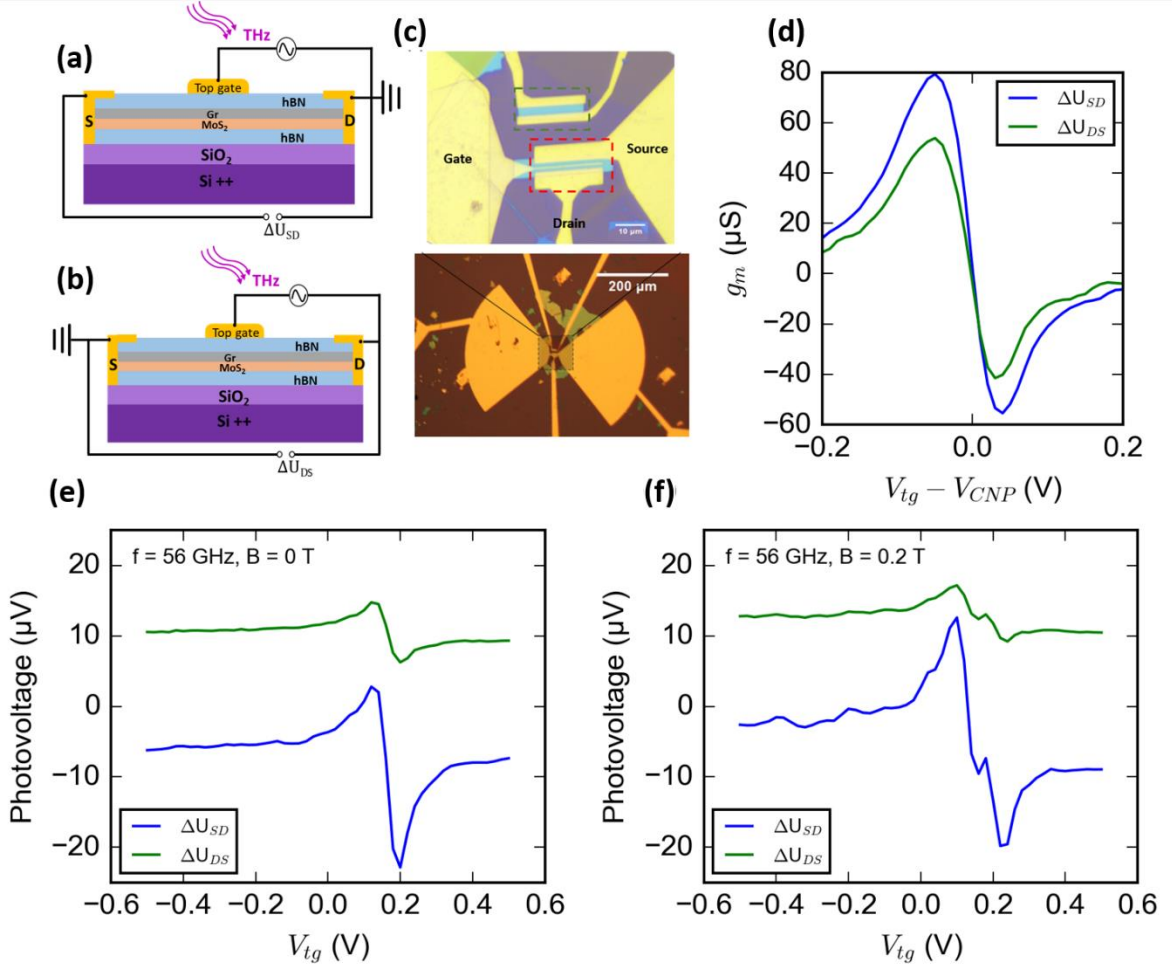


**Figure 1:** (a) Illustration of the device structure. For characterization, the rectified dc photovoltage ( $\Delta U_{SD}$ ) was measured between the source and drain terminals under THz illumination. (b) The same device structure with reversed measurement polarity ( $\Delta U_{DS}$ ). (c) Optical image showing the fabricated device with antennas for enhanced THz coupling. The red dashed square indicates the area of MoS<sub>2</sub>/Gr. (d) Transconductance ( $g_m$ ) as a function of gate voltage ( $V_{tg}$ ) for two measurement configurations:  $\Delta U_{SD}$  (blue curve) and  $\Delta U_{DS}$  (green curve), measured with a source-drain voltage  $V_{SD} = 20$  mV and a back-gate voltage  $V_{bg} = 0$  V, at a temperature  $T = 2$  K. The charge neutrality point (CNP) is observed around  $V_{tg} = 0.2$  V. (e) and (f) show the photovoltage response under 56 GHz illumination at a temperature of 2 K without and with magnetic field ( $B = 0.2$  T), respectively. In both figures, two measurement configurations are presented:  $\Delta U_{SD}$  (blue curve) and  $\Delta U_{DS}$  (green curve), corresponding to different grounding schemes of the source and drain terminals. The  $\Delta U_{SD}$  configuration exhibits a high photoresponse around the charge neutrality point (CNP), while the  $\Delta U_{DS}$  configuration shows a higher offset compared to  $\Delta U_{SD}$  and a lower signal around the CNP. These contrasting behaviours highlight an asymmetry in our device's photoresponse.

## Asymmetric photovoltage offset

A noticeable asymmetry in the photovoltage signal taking the form of a gate-voltage independent offset is observed when the source and drain are interchanged. However, most FETs used as THz detectors suffer from an inherent structural asymmetry between the source and drain. Coupling an incident THz radiation through an antenna placed between the source and gate creates indeed an asymmetry in signal feeding, which generates the photovoltage signal [39]. Shabanov et al. [40] demonstrated that positioning the gate asymmetrically near either the source or drain concentrates electromagnetic energy at one of the rectifiers, also causing signal asymmetry. In our sample however, the gate is centrally positioned, so it cannot account for the observed effect. The asymmetric signal could potentially be explained by the electron temperature gradient induced by the incident THz radiation and causing electron diffusion. When the 2D electron system is non-uniformly heated, its thermal and electrical properties are modified. This temperature gradient can appear because of the non-zero Seebeck coefficient of the graphene/MoS<sub>2</sub> or because of the electrical contact between two materials with different Seebeck coefficients [41]. The asymmetric feeding introduced by dissimilar contact geometries (antenna on the source side) could then result in a net current through the photo-thermoelectric effect, as shown for example in [42,43]. In the absence of an applied dc bias in the channel, the bolometric effect is expected to be negligible compared with the Seebeck effect [44] which is often observed in graphene- based devices [45, 46, 47, 48]. Based on the measured conductance at 1.7 K, we calculated the Seebeck coefficient with respect to the Fermi energy, which is controlled by the gate voltage (see Supplementary Materials, Fig. SM3). One finds that it is on the range of a few  $\mu\text{V}/\text{K}$ , and reaches its maximum value close to  $V_g = 0 \text{ V}$ . It becomes clear that a thermoelectric effect cannot happen in the region of the channel controlled by the top gate. However, the Seebeck effect could still account for an offset voltage of a few  $\mu\text{V}$ , since an electronic temperature increase of a few Kelvins could happen with the rather high power used in this experiment. The fact that this offset is independent of the gate voltage points toward a Seebeck signal originating at the metal-graphene interface, far from the top gate. The difference of the offset voltages measured at the source and drain confirms this interpretation: we expect different temperature rises at the two interfaces, due to different coupling with the Gigahertz wave on each side of the channel. Other sources of asymmetrical voltages, associated for example with asymmetry in the current leakage path under the back gate, cannot be ruled out entirely.

## Magnetic field results

When a magnetic field is applied perpendicular to the layers, the source-drain photovoltage signal as a function of the magnetic field reveals Shubnikov-de Haas-like oscillations, which have been observed in several different materials [49, 50, 51, 52, 53]. This non-resonant signal is especially pronounced in the  $\Delta U_{\text{SD}}$  configuration, which depends on the gate voltage and related to the rectification of the incident electromagnetic wave via overdamped plasma waves in the transistor channel. The photovoltage signal

thus mirrors the changes in electronic gas conductivity caused by the Fermi level oscillating between Landau levels in response to the magnetic field. The raw curves as a function of magnetic field are provided in Fig 2(a) as a waterfall plot for different gate voltages for sake of clarity. Figure 2(c) shows a colorplot of the second derivative of the signal to emphasize the oscillatory behavior of the signal.

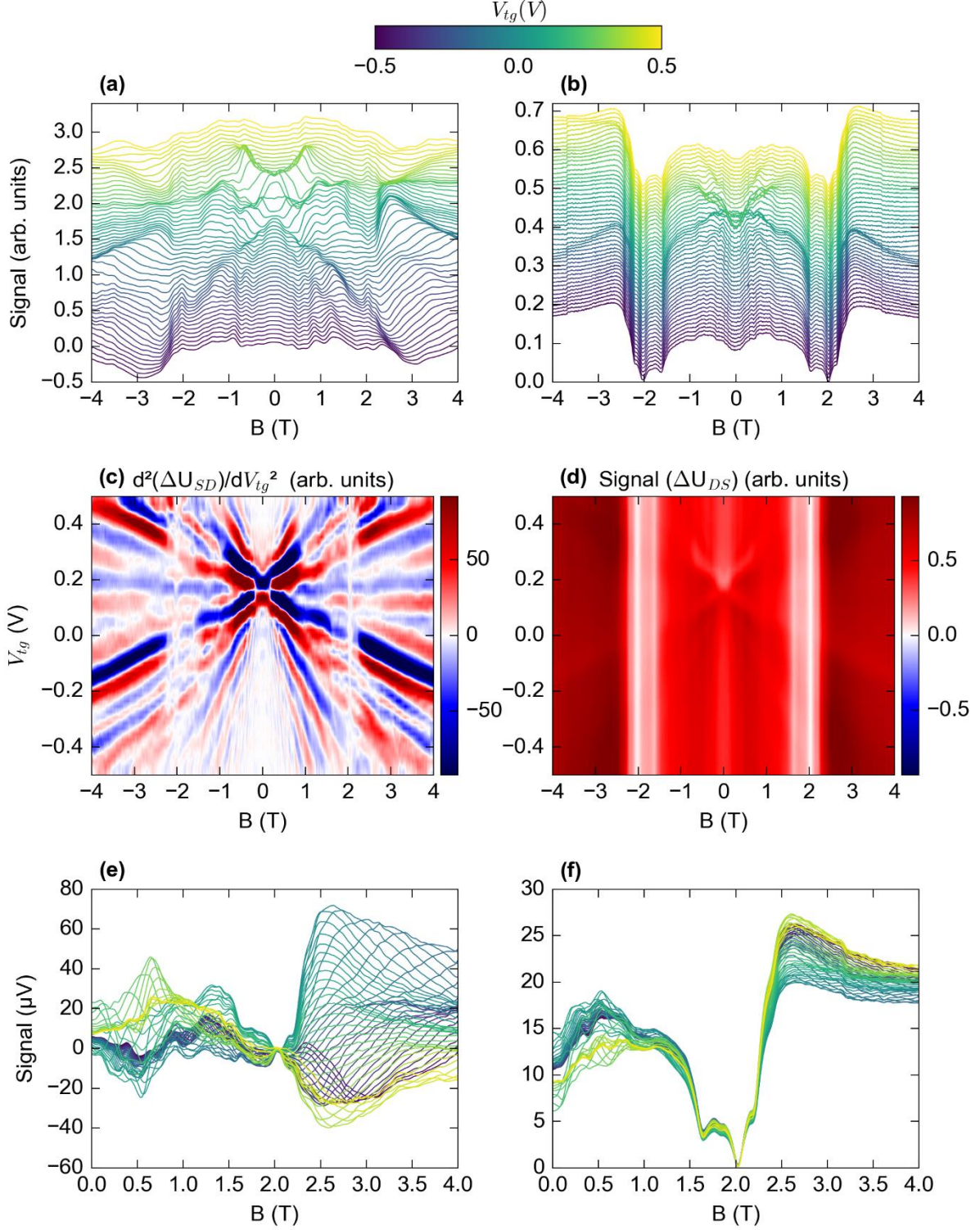


**Figure 2:** (a) Waterfall plot of photovoltage versus magnetic field for various top gate voltages as indicated by the colorbar in the  $\Delta U$  (source-drain) configuration at 1.7 K and under excitation at 56 GHz. (b) Waterfall plot similar to the one in panel (a) for the  $\Delta U_{DS}$  (drain-source) configuration. (c) Colormap of  $d^2\Delta U_{SD}/dV_{tg}^2$  for the (source-

drain) configuration, showing pronounced X-shaped Shubnikov-de Haas-like oscillations. **(d)** colormap for  $\Delta U_{DS}$  configuration, with pronounced ESRs. **(e)** Photovoltage vs. magnetic field for different top gate voltages for  $\Delta U_{SD}$  configuration and **(f)** for  $\Delta U_{DS}$  configuration.

As seen in Fig. 2(e), there are several well visible resonances in the range between  $B = 1.5$  and  $2.5$  T overlapping with the Shubnikov-de Haas-like oscillations that are especially clear in the source-drain (SD) configuration. These resonances, at a fixed frequency, are independent of the magnetic field and carrier density. In the drain-source (DS) configuration, which is almost independent of the gate voltage, these resonances become clearer, even though their amplitude is slightly lower than in the SD configuration. This overall resonant signal is attributed in both cases to the spin-flip transitions between the Zeeman splitted spin subbands of conduction band.

## Discussion

### 1) Interpretation of the magnetic resonances

Spin-orbit coupling in graphene can be enhanced by the presence of a transition metal dichalcogenide substrate with strong spin-orbit coupling [54, 55]. Monolayer MoS<sub>2</sub> presents promising potential in this context, theoretically providing substantial enhancements in spin-orbit coupling without affecting graphene's electronic transport properties. Previously the fine structure of the spin-orbit coupling in the Dirac bands of graphene on monolayer MoS<sub>2</sub> was theoretically studied through first-principles calculations [34]. One of the objectives of this work was to induce and measure a stronger spin-orbit coupling in this few atomic layer heterostructure compared to that in isolated graphene samples. As seen from Fig. 3, the resulting curves contain four electronic spin resonances as shown in the inset of. These ESRs whose frequency evolves linearly with the magnetic field (see Fig. 3) were studied as a function of the incident excitation frequency up to 115 GHz. The first resonance marked as  $\alpha$ , extrapolating to zero energy at zero magnetic fields, is attributed to the spin-flip transition between the Zeeman split subbands from the same valley and can be fitted with a Landé g-factor of 2.09 calculated from its slope. This ESR has been previously observed through GHz photovoltage in Ratchet sensors and graphene-based p-n junctions detectors [56]. By extrapolating the other resonances to zero fields, three zero field splittings (ZFSs) are revealed. One of them, named  $\beta$ , is due to the intrinsic spin-orbit coupling with a frequency of about 11 GHz (corresponding to an energy of 44.5  $\mu$ eV, comparable to previously obtained values), while the two others are attributed to sublattice potential with the values also comparable to those reported in the literature [57, 58, 59], i.e.,  $\Delta\gamma' \approx -4$  GHz (corresponding to an energy of about -16.5  $\mu$ eV), and  $\Delta\gamma \approx 5.6$  GHz (corresponding to 23  $\mu$ eV).

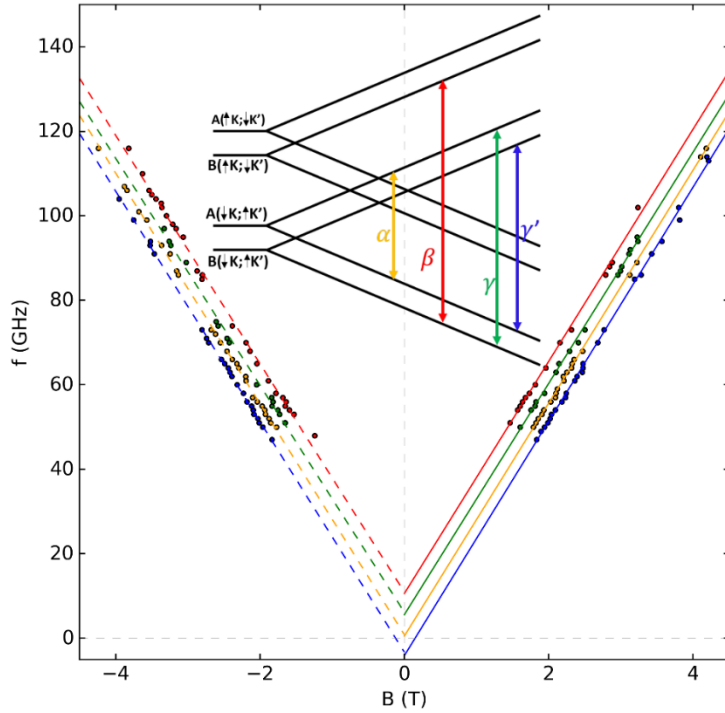


**Figure 3:** Position of ESRs as a function of the magnetic field and frequency. Four distinct resonances are marked as  $\gamma'$  (blue),  $\alpha$  (orange),  $\gamma$  (green), and  $\beta$  (red). Solid and dashed lines represent extrapolations for positive and negative magnetic field, respectively. In the inset a schematic diagram illustrates the energy levels and allowed transitions in graphene under an applied magnetic field. It depicts four energy levels representing different spin and valley states, labeled as  $A(\uparrow K; \downarrow K')$ ,  $B(\uparrow K; \downarrow K')$ ,  $A(\downarrow K; \uparrow K')$ , and  $B(\downarrow K; \uparrow K')$ . The diagram shows the possible resonance transitions indicated by colored arrows:  $\alpha$  (orange),  $\beta$  (red),  $\gamma$  (green), and  $\gamma'$  (blue).

Surprisingly, roughly the same values found in several other graphene samples appear to be independent of the presence of the MoS<sub>2</sub> layer. Moreover, similar results were obtained in magic-angle twisted bilayer graphene [60] and were interpreted as due to some collective excitations linked to the correlated states in magic angle bilayer graphene. However, those results were commented by L. Tiemann et al. [61], arguing that identical resonance features have already been reported in previous works on mono- and few-layer graphene. As an explanation for the experimental results, it was suggested that twisted bilayer graphene may create a slight asymmetry between the two sublattices, similar to that observed in CVD-grown samples in [62]. In our device, interestingly, the sample fabrication method is different, but the ZFS values are similarly consistent with those reported previously (see Fig. 3). The explanation of this intriguing result requires further research beyond the scope of this work and will be the subject of future studies. Importantly, tight-binding modelling shows that both the magnitude and the type of proximity induced SOC between graphene and MoS<sub>2</sub> strongly depends on the Moiré angle between the two materials [63]. This twisted angle is not controlled in our case and is therefore unlikely to correspond to an optimal situation.

## 2) Origin of the ESR photovoltage



The PV-ESR signal in graphene-based structures has been previously explained by Bray et al. [34] by the resonant microwave absorption at the spin-flip transition energy, similarly to the commonly used EDESR technique. Alternatively, it was also mentioned that the mechanisms of spin-to-charge conversion, namely spin-dependent scattering, tunnelling, and recombination [64] may also be at the origin of this PV-ESR signal. Interestingly, as will become clear below, our results highlight that the PV-ESR signal represents a photovoltage drop, regardless of the signal's sign (cf. Fig. 2(e)). Even though it is still impossible to draw conclusions about the exact origin of the signal, these results already provide a better understanding of previous findings [23,65], where the ESR signal seemed to change sign erratically. This section therefore presents a non-exhaustive list of probable interpretations of the origin of ESR signal in the photovoltaic or photoconductive regime.

On the DS measurement configuration, the shape of the magnetic field induced photovoltage  $\Delta U_{DS}$  changes drastically with respect to  $\Delta U_{SD}$ . SdH-like oscillations are still present, but they are about one order of magnitude weaker in amplitude. In contrast, the ESR signal remains on the same order of magnitude and largely dominates the spectra, revealing very distinct transitions that allow for detailed and reliable analysis, as shown in Figs. 2(b), 2(d) and 2(f). As in  $\Delta U_{DS}$ , the ESR signal manifests as a significant drop in the photovoltage and the overall signal even almost cancels out at  $B = 2$  T. The overall ESR signal amplitude is comparable to that in  $\Delta U_{SD}$ . The main differences are that the signal remains consistently positive, shows a weak dependence on the gate voltage, and the SdH-like oscillations are scarcely visible, causing minimal signal distortion. Such a behavior arises because the source-drain signal has a different physical origin from non-resonant plasma wave rectification obtained in the source-drain configuration. As discussed in the first part of this section, the signal exhibits a strong gate voltage independent offset, already visible at zero magnetic field. This evidences a stronger thermoelectric effect affected the ESR, while the weaker damped plasma contribution is consistent with weaker SdH-like oscillations. This thermoelectric effect is likely of Seebeck origin, since it is symmetric in magnetic field.

The ESRs appear again as a significant reduction in the photovoltage, and even as an almost complete collapse at  $B = 2$  T in both  $\Delta U_{SD}$  and  $\Delta U_{DS}$ . Indeed, even in  $\Delta U_{SD}$ , it is evident that the signal tends to zero, regardless of its initial polarity. To confirm this assumption, photoconductivity measurements were also performed by injecting a current into the transistor channel in the  $\Delta U_{DS}$  configuration at 56 GHz. Regardless of the baseline signal's polarity or magnitude, which varies with the applied current, the photoconductivity also consistently drops towards zero (See Supplementary Materials, Figure SM 4,5).

It turns out that this behaviour of the photoconductivity signal was already observed in various systems. Already in the 1970s, Lépine [66] measured a decrease in the photoconductivity of silicon samples subjected to powerful microwaves and a magnetic field swept through ESR. This drop of photoconductivity was later observed by several other groups [67, 68, 69, 70] and explained by a spin-

dependent recombination process, in which the recombination rate of the carriers depends on their spin polarization. Consequently, any variation in the spin polarization of the system would affect the recombination time. The steady-state excess carrier concentration  $\delta n$  is related to the generation rate  $G$  and recombination time  $\tau$  by  $\delta n = G\tau$ . The change in excess carrier concentration is therefore directly related to the change in photovoltage  $\delta U$  through the following equation:  $\delta U = \delta n e \mu$ , where  $e$  is the elementary charge and  $\mu$  is the carrier mobility. Consequently, a decrease in  $\tau$  leads to a decrease in  $\delta n$ , resulting in the observed drop in photovoltage.

In more details, Lépine's initial idea was to explain the observed drop of photoconductivity as due to the spin polarization of conduction electrons and paramagnetic recombination centers in the presence of a DC magnetic field. However, this model predicted changes in recombination rates that were several orders of magnitude smaller than those observed experimentally. Alternatively, the Kaplan–Solomon–Mott explanation [71], based on the Shockley–Read–Hall recombination process and consistent with most experimental observations, suggests that the initial spin polarization arises from the creation of electron-hole pairs trapped at recombination centers before they eventually recombine. An illustration of this idea is sketched in Fig. 4. The photoexcited electron-hole pairs in singlet configuration have a shorter lifetime than those induced in triplet configuration. Therefore, the steady-state population of singlet pairs would be smaller, resulting in an excess of triplet configurations that occupy the recombination centers and inhibit further recombination (see Fig. 4(b)). Exciting the system at the ESR frequency returns the recombination centers to a random spin distribution, which contains more singlet states (see Fig. 4(c)), thus reducing the recombination time. Since the concentration of photo-created carriers is a function of the recombination time, and because photoconductivity is proportional to the concentration of photocarriers, a decrease in photoconductivity should occur when the magnetization of the system is reduced.

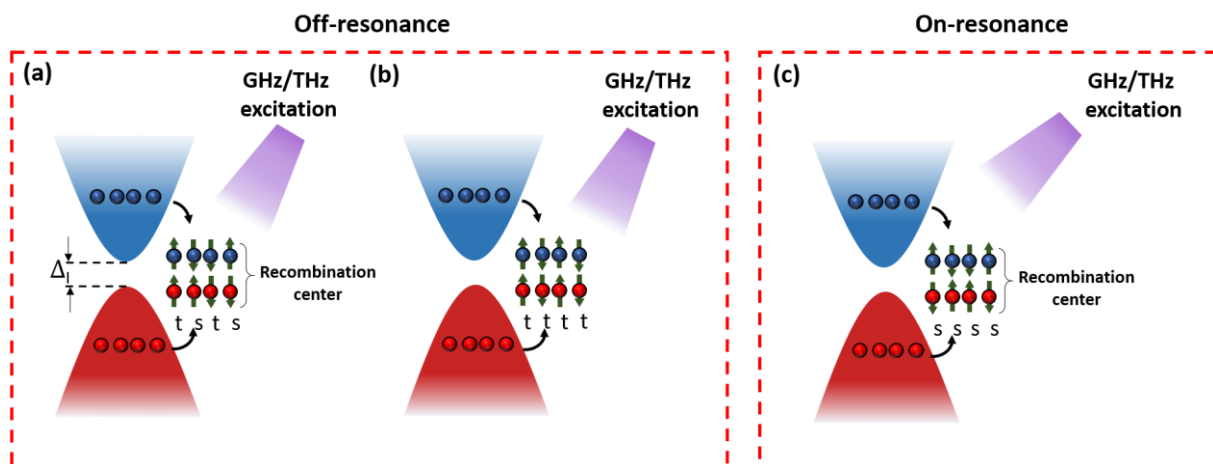


**Figure 4:** Representation of the Kaplan–Solomon–Mott explanation [67] of spin-dependent recombination adapted to graphene: (a) electron–hole pairs are captured at recombination centers, with singlet pairs rapidly recombining, (b) leading to an accumulation of triplet pairs; (c) electron spin resonance excitation increases the number of singlet pairs, thereby reducing the recombination time.

Although graphene does not exhibit a spin-dependent recombination mechanism identical to the Shockley–Read–Hall process, as it has only a tiny energy gap, our first phenomenological approach is based on the fact that defects and impurities [72], which create localized states in graphene, can act as spin-dependent recombination centers [73, 74, 75], similar to those in conventional semiconductors. In a phenomenological way the electron-density-dependent mechanism of photovoltage signal suppression can be described as follows. Let us assume two electron species (e.g., spin-up and spin-down electrons or, possibly triplet and singlet configurations of electron-hole pairs) with the sheet densities  $n_1, n_2$  determined by a balance between (equal for the two species) generation and recombination rates, so that  $Gt_1 = n_1$ ;  $Gt_2 = n_2$ . The total density  $n = n_1 + n_2 = G(t_1 + t_2)$  determines the photovoltage signal. In the case of ESR resonance the occupation numbers of the two species are being equalized, which can be described via the following system of rate equations:

$$\begin{aligned} \frac{dn_1}{dt} &= G - \frac{n_1}{t_1} - \frac{n_1 - n/2}{t_{12}} \\ \frac{dn_2}{dt} &= G - \frac{n_2}{t_2} - \frac{n_2 - n/2}{t_{12}} \end{aligned}$$

where  $t_{12}^{-1}$  is a characteristic rate for equilibration of the densities at ESR, this rate is assumed to be fast as compared to the stationary recombination rates:  $t_{12} \ll t_1, t_2$ .

Solving for a stationary state one gets  $n = n_0 \frac{4x}{(1+x)^2}$ , where  $n_0 = G(t_1 + t_2)$  is the stationary

density in the absence of ESR resonance, and  $x = t_2/t_1$ . At any  $x \neq 1$ , i.e. if the recombination rates for the two species are unequal, this formula suggests a reduction of the total density due to the equilibration of the occupations of the two species. The physics behind this effect is straightforward and quite general: ESR reduces the lifetime of the longer-living species by redistributing them into the fast recombination channel. However, this model does not fully correspond to our experimental technique. Indeed, unlike the conventional EDESR technique, our photovoltage or photoconductivity technique does not involve resonant absorption, but rather Drude absorption. On the other hand, charge density oscillations are induced by this incident radiation, and the resulting rectification signal arises from the simultaneous modulation of electron velocity and carrier

density at the source and gate contacts, respectively. Thus, even if the average electron density remains constant, the density fluctuates due to the oscillatory motion of the electron gas, leading to a nonequilibrium distribution of electrons (with regions of excess and deficit). Excess electrons from regions of high electron density may be trapped at recombination centers and then either recombine or be released due to the nonequilibrium nature of the plasma waves, depending on their lifetime within the traps.

It is generally believed that only spin-dependent recombination should lead to a reduction in photovoltage [76], even if it has been theoretically demonstrated in silicon transistors [77] that spin-dependent scattering mechanisms could also lead to a reduction in conductivity when the process is determined by virtual transitions into doubly occupied donor states. In what follows, we consider an alternative approach that could also result in a reduction of the photovoltage signal during ESR resonance. Indeed, apart from spin-dependant recombination, another mechanism responsible for the observed decrease of the PV-ESR signal might originate from an effect of the ESR on scattering and damping channels without changing the stationary electron density. Electrons can indeed be scattered by neutral donors for example, and since both have spins, the scattering will depend on whether the spins are parallel (triplet) or anti-parallel (singlet), similar to what was previously discussed regarding spin-dependent recombination processes. Let us consider two scattering processes characterized by the time constants  $t_1, t_2$ , characterizing spin-conserving and spin-flip scattering, respectively, the total scattering time  $t$  is given by  $t^{-1} = t_1^{-1} + t_2^{-1}$ . The spin-flip scattering time can be estimated as

$$t_2^{-1} = \frac{p}{h} \sum_{\mathbf{k}, \mathbf{k}'} \mathbf{a}_{\mathbf{k}, \mathbf{k}'} |V_{\mathbf{k}\mathbf{k}'}|^2 \sin^2 \theta_{\mathbf{k}\mathbf{k}'} D(w),$$

where  $V_{\mathbf{k}\mathbf{k}'}$  is the matrix element describing the scattering,  $\mathbf{k}, \mathbf{k}'$  are the initial and final electron wavevectors  $\theta_{\mathbf{k}\mathbf{k}'}$  is the angle between them,  $D(w) = \frac{1}{p} \frac{\Gamma}{(d_{SO} - hw)^2 + \Gamma^2}$  is a Lorentzian function describing resonance with a width  $\Gamma$  centered at the spin-

orbit splitting  $d_{SO}$  characterizing the energy difference between spin-up and spin-down states. In the context of a simplified phenomenological description, we express the resonant spin-flip time in terms of spin-conserving time through a constant parameter  $x$  and the resonant factor  $D(w)$

$$t_2^{-1} = t_1^{-1} x D(w).$$

The total inverse scattering time would then be  $t^{-1} = t_1^{-1} (1 + x D(w))$  exhibiting a resonant maximum at a frequency  $w = d_{SO}$ . The resonant increase in the scattering rate would lead to greater damping of the plasma oscillations and reduced conductivity, resulting in a decrease in the photovoltage signal.

Based on our results, we are unable to distinguish between these two spin-dependent phenomena. Nevertheless, the systematic decrease of the measured signal of spin resonances indicates that the PV-ESR likely stems from a spin-charge conversion phenomenon linked to spin-dependent recombination or scattering. When the sample is excited at the ESR frequency, the spin polarization is reduced, which decreases the recombination or scattering time and consequently lowers the photovoltage. Regardless of the origin of the photovoltaic or photoconductive signal — whether it is due to a ratchet effect, a thermoelectric effect, rectification by a p-n junction, or plasma waves — this signal is consistently reduced when ESR is excited. Recent ESR results obtained by Hild and coworkers [78] in ratchet detectors based on graphene metamaterials also showed a reduction in the total signal. Our current results show that the origin of the ESR signal in their work was mistakenly attributed to a Seebeck effect rather than a spin-dependent phenomenon.

### 3) Resonances Analysis

In the following, we investigate the effect of incident optical power on the photovoltage signal (see Fig. 5a) by considering the two proposed phenomena of spin-dependent scattering and recombination. Firstly, as seen in Fig. 5(b), the total signal outside of the ESR, evolves linearly with the incident power. Figure 6 then reveals that the ratio of the total signal to the ESR signal under resonant conditions increases at low power and saturates already above 20 mW. A similar result is obtained in both SD and DS configurations, regardless of the origin of the total signal—whether it is due to plasma waves or a Schottky effect.

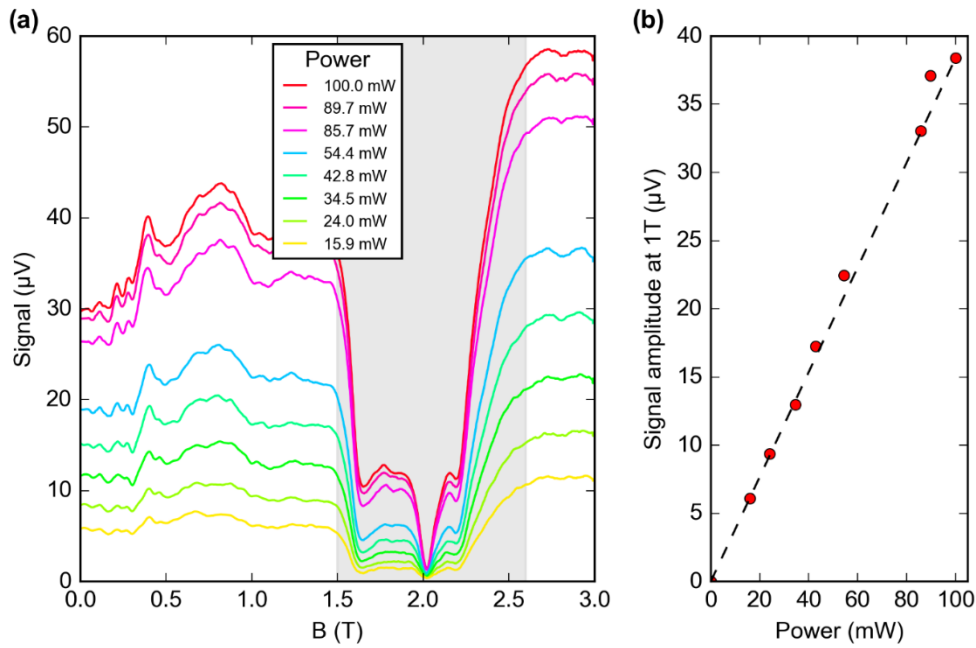


**Figure 5:** Power dependence of the photovoltage signal in the drain-source ( $\Delta U_{\text{DS}}$ ) configuration at 56 GHz with an injected current of  $5 \mu\text{A}$  at a temperature of 2 K. **(a)** Photovoltage signal as a function of magnetic field for

different incident powers. The gray shaded area highlights the region between 1.5 and 2.6 T where a significant signal drop is observed. **(b)** Signal amplitude at 1 T versus incident power, showing a linear relationship. The dashed line serves as an eye guide for the linear trend.

If we analyse these results considering the effect of spin-dependent scattering as responsible for the photovoltage drop, we can emphasize the role of the electric field generated by the incident radiation at the drain and source contacts, which may influence the spin scattering rate. However, given the weak spin-orbit coupling in graphene, an in-plane electric field should result in only a minor increase in spin depolarization. The Rashba effect may contribute to a slight decrease in the photovoltage, as the accelerating electric field tends to enhance spin depolarization. However, a saturation effect is not expected in this context. This approach, which presents several weaknesses, thus needs a more thorough theoretical assessment.

In the context of spin-dependent recombination, it is possible to analyze the efficiency of spin-flip processes or other resonance-induced phenomena. This is typically measured by the intensity of the ESR signal. With sufficient power, gigahertz excitation generates photo-carriers that reduce the population differences between spin states, potentially saturating the transitions and cancelling the photovoltage. This saturation phenomenon typically occurs due to the spin-lattice relaxation (relaxation time  $T_1$ ), particularly when the concentration of unpaired electrons is low or at low temperatures [79]. The mechanisms by which the spin-lattice interactions can take place all involve interactions of the spin system with phonons [80]. The spin-spin relaxation time  $\tau_s$  can also be deduced from the full width at half maximum of the ESR signal which is directly related to spin decoherence (See Supplementary Materials - Figure SM 6). Using the following equation  $\tau_s = \hbar \left( 2h \frac{\Delta f}{\Delta B} \delta B \right)^{-1}$  [34], where  $\hbar$  is the reduced Planck constant,  $h$  is Planck's constant,  $\Delta f/\Delta B$  is the slope of the resonance, and  $\delta B$  is the full width at half maximum of the resonance peak, we calculate the spin relaxation time for the  $\alpha$  resonance.

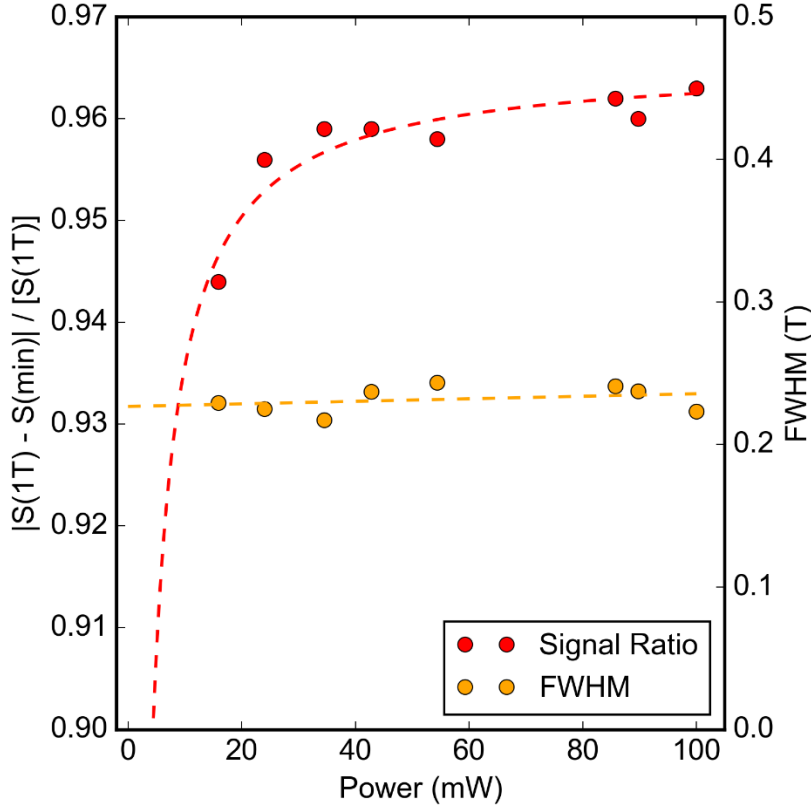


**Figure 6:** Power dependence of the signal intensity at the center of the resonance. The left y-axis shows the signal intensity  $|S(1T) - S(\min)| / [S(1T)]$ . The right y-axis displays the full width at half maximum (FWHM) (orange symbols) and its corresponding fit (orange lines). All parameters are plotted against the microwave power in mW. The signal intensity data is fitted using a saturation curve model:  $y = aP / (1 + bP)$ , where  $P$  is the microwave power and  $a$ ,  $b$  are fitting parameters. The FWHM is fitted with a power-dependent broadening model:  $\text{FWHM} = c\sqrt{(1 + aP)}$ , where  $c$  and  $a$  are fitting parameters.

The fits described by the following equations yield key insights into the system's behavior. For the signal intensity, we employ a saturation curve model of the form  $aP/(1 + bP)$ , where  $P$  is the microwave power, and  $a$  and  $b$  are fitting parameters. The full width at half maximum ( $\delta B$ ) is fitted with a power-dependent broadening model:  $\delta B = c\sqrt{(1 + aP)}$ , where  $c$  is a fitting parameter. From these fits, we obtain the saturation power (approximately 5-10 mW), maximum signal intensity (around 0.95), and intrinsic linewidth (about 0.23 T which corresponds to  $\tau_s = 12.5$  ps). These spin relaxation values are in good agreement with previous results in the literature [34, 59]. The low saturation power indicates high sensitivity of the sensor to GHz excitation. The relatively stable  $\delta B$  across the power range implies that inhomogeneous broadening dominates in this system.

## Conclusion

Using a graphene/MoS<sub>2</sub> field-effect transistor as a THz/GHz detector, we observed four electronic spin resonances in the photovoltaic signal measured as a function of the magnetic field between 55 and 115 GHz. These resonances are attributed to intrinsic spin-orbit coupling for one, sublattice potential for two others, and to the spin-flip transition between the Zeeman split bands with a Landé g-factor of 2.09 for the last one. Interestingly, compared to results from the literature on monolayer graphene samples on various substrates, the ZFS values we measured do not seem to be affected by the presence of the MoS<sub>2</sub> layer. This intriguing result will need to be studied in greater detail, both theoretically and experimentally. Additionally, although we anticipated a plasma wave signal in our transistor-based detector, an unexpected Seebeck rectification signal was observed. This finding revealed that the spin resonances consistently appear as a decrease in the signal, regardless of its origin or polarity. While we cannot definitively determine whether the phenomenon responsible for this effect is spin-dependent scattering or spin-dependent recombination, we interpret the observed signal drop phenomenologically as the system returns to a random spin distribution during ESR excitation. These findings enhance our understanding of photovoltaic detection of the ESR signal in graphene-based GHz/THz detectors. They also highlight the efficiency and potential of these optimized sensors for investigating spin, topological, and proximity phenomena in two-dimensional quantum materials.

### **Acknowledgements**

This work was supported by the Terahertz Occitanie Platform. We also acknowledge the Institute for Quantum Technologies in Occitanie (IQO) and the Occitanie Region for their support through a doctoral fellowship. Additional funding was provided by the French Agence Nationale de la Recherche (ANR) under the Jedi project (JCJC, ANR-18-CE24-0004), the France 2030 program through Equipex+ (Hybat project, ANR-21-ESRE-0026) and PEPR Electronique (Comptera project), as well as by the European Union under the Flag-Era JTC 2019 (DeMeGRaS project, ANR-19-GRF1-0006). J.A.D.-N. thanks the support from Junta de Castilla y León co-funded by FEDER under the Research Grant numbers SA103P23 and from the Universidad de Salamanca for the María Zambrano postdoctoral grant funded by the Next Generation EU Funding for the Requalification of the Spanish University System 2021–23, Spanish Ministry of Universities. Y.M.M acknowledge the support from the Ministry of Science and Innovation (MCIN) and the Spanish State Research Agency (AEI) under grants (PID2021-126483OB-I00).

### **Author contributions**

The experiment was proposed by FT. SN, KD, CB, KM and FT discussed the experimental data and interpretation of the results. The samples were fabricated by KD, JDN and SN. THz photoconductivity



experiments were carried out by KD, CB and CC. Characterization measurements were conducted and analysed by BJ, KD, SN, YMM, MP and SR. KM, KD and CB handled the data and prepared the figures. FT wrote the manuscript and all co-authors corrected it.

## Competing interests

The authors declare no competing financial interests.

## Data availability

Data are available upon reasonable request to the corresponding author. Dataset will also be uploaded on the Recherche Data Gouv repository (<https://recherche.data.gouv.fr>) once the manuscript is accepted and published.

## Supplementary Material

### - Raman spectroscopy and photoluminescence characterization

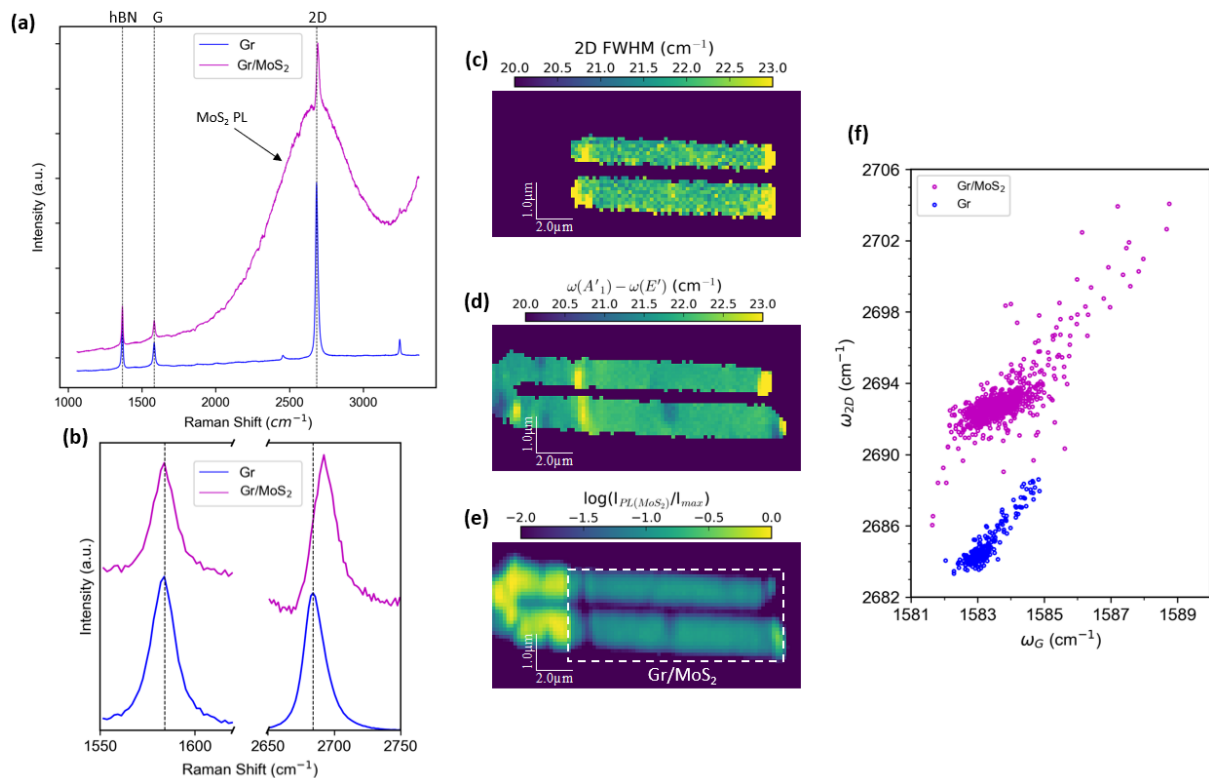


**Figure SM 1:** Raman and photoluminescence measurements of the graphene (Gr) and graphene–MoS<sub>2</sub> (Gr/MoS<sub>2</sub>) encapsulated in hBN structures. **(a)** Average Raman spectra extracted from Raman maps (not shown) of the Gr with (magenta line) and without (blue line) MoS<sub>2</sub> devices, showing characteristic monolayer graphene and hBN Raman bands as well as MoS<sub>2</sub> photoluminescence (PL). **(b)** Zoom of (a) in the G and 2D regions (after intensities normalization), highlighting the 2D band upshift in the presence of MoS<sub>2</sub>. **(c)** Graphene 2D band full width at half maximum (FWHM) map of the Gr/MoS<sub>2</sub> device compatible with a homogeneous monolayer graphene. **(d)** MoS<sub>2</sub> frequency difference between A'<sub>1</sub> and E' modes ( $\Delta\omega$ ) map of the Gr/MoS<sub>2</sub> device compatible with monolayer MoS<sub>2</sub>. **(e)** MoS<sub>2</sub> PL intensity map (colorbar in log-scale) of the Gr/MoS<sub>2</sub> device showing a one order of magnitude PL quenching in graphene's presence (the Gr/MoS<sub>2</sub> region is indicated by the white dashed rectangle, the

yellow part on the left of the map being a MoS<sub>2</sub> region without graphene). **(f)** Correlation between the graphene 2D band ( $\omega_{2D}$ ) and G band ( $\omega_G$ ) positions for Gr/MoS<sub>2</sub> (magenta filled dots) and Gr (blue filled dots) devices extracted from respective Raman maps (not shown). Each point in the plot corresponds to a different position on the samples.

The Raman spectra presented in Fig. SM1(a) are the averages obtained from Raman maps of hBN encapsulated devices of graphene with (magenta line) and without (blue line) MoS<sub>2</sub>. Both spectra exhibit a sharp 2D band compatible with monolayer graphene. Fig. SM1(b) shows a close view of the G and 2D band regions of the spectra of Fig. SM1(a) after intensities normalizations, revealing a 2D band upshift in the presence of MoS<sub>2</sub> which has been shown to be a signature of the coupling between the transition metal dichalcogenide layer and graphene (see Fig. 7a in [83]). For the graphene–MoS<sub>2</sub> device, the homogeneity of the monolayer graphene is confirmed through the map of the 2D band's full width at half maximum (FWHM) presented in Fig. SM1(c) as well as the map of the G band integrated intensity (not shown). Evidence of monolayer MoS<sub>2</sub> is provided in Fig. SM1(d), which shows a map of the frequency difference between the A'<sub>1</sub> and E' modes ( $\Delta\omega = \omega(A'_1) - \omega(E')$ ). Fig. SM1(e) presents a MoS<sub>2</sub> photoluminescence (PL) intensity map (with a colorbar in log-scale normalized to the maximum intensity of the map), where a one order of magnitude MoS<sub>2</sub> PL quenching in graphene's presence (corresponding to the region within the white dashed rectangle) as compared to the MoS<sub>2</sub> region without graphene observed on the left part of the map. Fig. SM1(f) shows the  $\omega_{2D}$  vs  $\omega_G$  correlations for graphene with (magenta filled dots) and without (blue filled dots) MoS<sub>2</sub> and further details the 2D mode upshift in the presence of MoS<sub>2</sub> as illustrated in Fig. SM1(b). In summary, the observed upshift of the 2D band of graphene in the presence of MoS<sub>2</sub> combined with the MoS<sub>2</sub> PL quenching in the presence of graphene is a signature of a strong coupling between graphene and MoS<sub>2</sub> [83].

- Source-drain and drain-source current

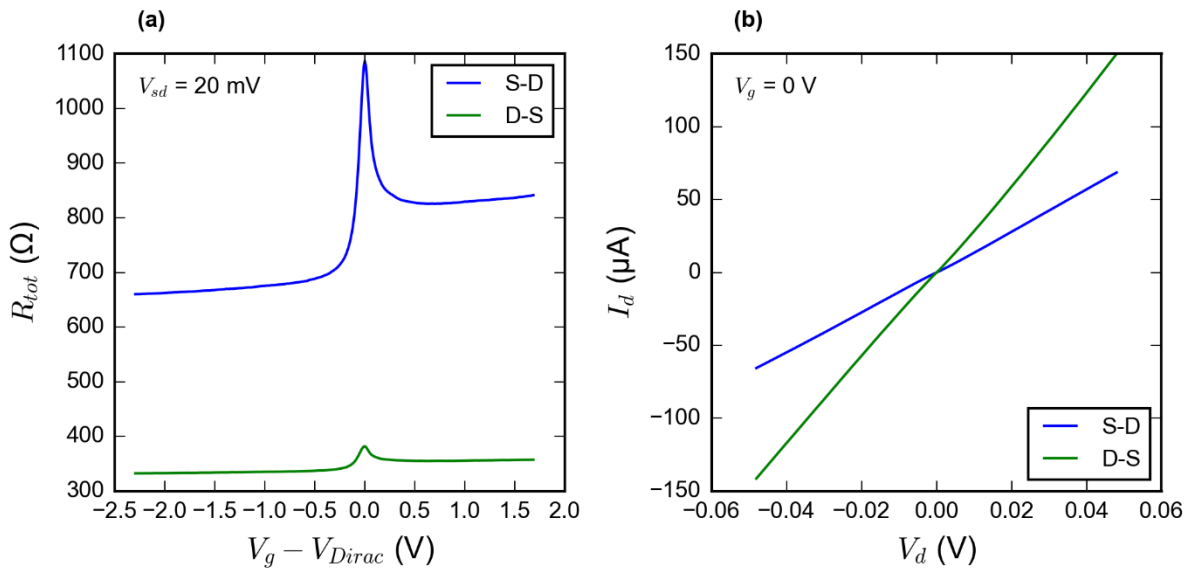


**Figure SM 2:** **(a)** Total resistance as a function of gate voltage relative to the Dirac point ( $V_{Dirac}$ ) for two measurement configurations at  $V_d = 20$  mV at  $T = 2$  K. Blue: source-drain, green: drain-source. **(b)** Drain current ( $I_d$ ) versus drain voltage ( $V_d$ ) for the same configurations at  $V_{tg} = 0$ .

- Seebeck coefficients

To quantify the contribution of the photo-thermoelectric (PTE) effect in our device, we can calculate the Seebeck coefficient ( $S$ ) using the Mott formula, which is particularly relevant for 2D materials. The Seebeck coefficient is given by:

$$S = -\frac{\pi^2 k_B T}{3e} \frac{1}{G} \frac{dG}{dE_F},$$

where  $k_B$  is the Boltzmann constant,  $T$  is the temperature,  $e$  is the elementary charge,  $G$  is the conductance, and  $E_F$  is the Fermi energy.

Figure 1 shows the calculated Seebeck coefficients for both  $\Delta U_{SD}$  and  $-\Delta U_{DS}$  configurations as a function of  $E_F$  at  $T = 1.7$  K. Both curves exhibit the characteristic 'S' shape expected for graphene, with the Seebeck coefficient changing sign near the charge neutrality point (CNP).

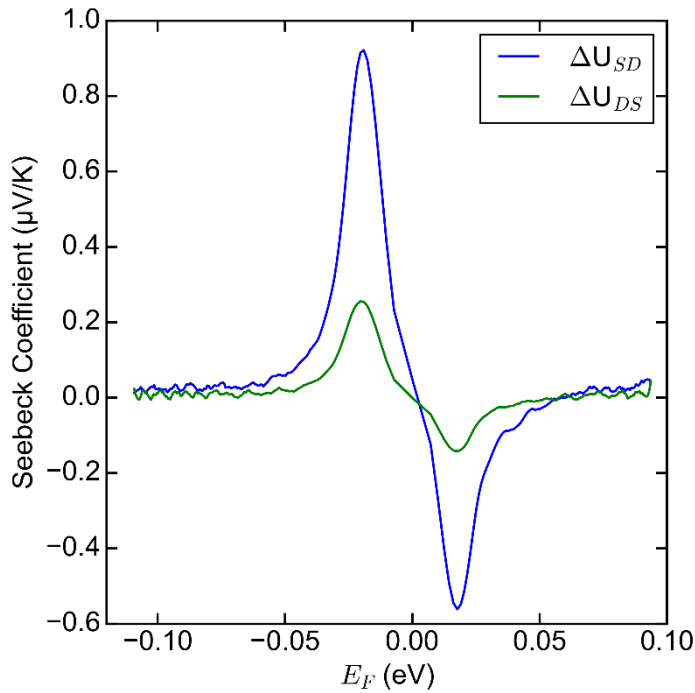


**Figure SM 3:** Calculated Seebeck coefficients as a function of Fermi energy for  $\Delta U_{SD}$  and  $\Delta U_{DS}$  configurations.

The model predicts a significant response only near the CNP, which does not fully align with our experimental results. This suggests that additional mechanisms are at play in our device's photoresponse.

#### - Effect of a direct current applied in the FET's channel

As demonstrated in the literature, a continuous current in the transistor channel can increase or decrease the asymmetry between the source and drain, and consequently the photovoltage, depending on the direction of the applied current [81]. Figure SM 2.a) shows a waterfall plot of the photovoltage measured in the  $\Delta U_{DS}$  configuration at 56 GHz, with injected current ranging from -5 to 5  $\mu\text{A}$ . The plot reveals a clear correlation between the injected current and the photovoltage offset. As we sweep from negative to positive current values, we observe a systematic shift in the photovoltage baseline. At 0 T the

photovoltage exhibits a marked asymmetry in response to current injection. Specifically, a  $-5 \mu\text{A}$  current results in a photovoltage of  $-7 \mu\text{V}$ , while a  $5 \mu\text{A}$  current produces a significantly larger response of  $30 \mu\text{V}$ . This asymmetry suggests a non-linear relationship between the injected current and the resulting photovoltage. Notably, we observe a distinctive behavior in the magnetic field region between 1.5 and 2.6 T. Regardless of the baseline signal's polarity or magnitude, the photovoltage consistently drops to 0 in this range. This drop to zero occurs independently of whether the overall signal is positive or negative.

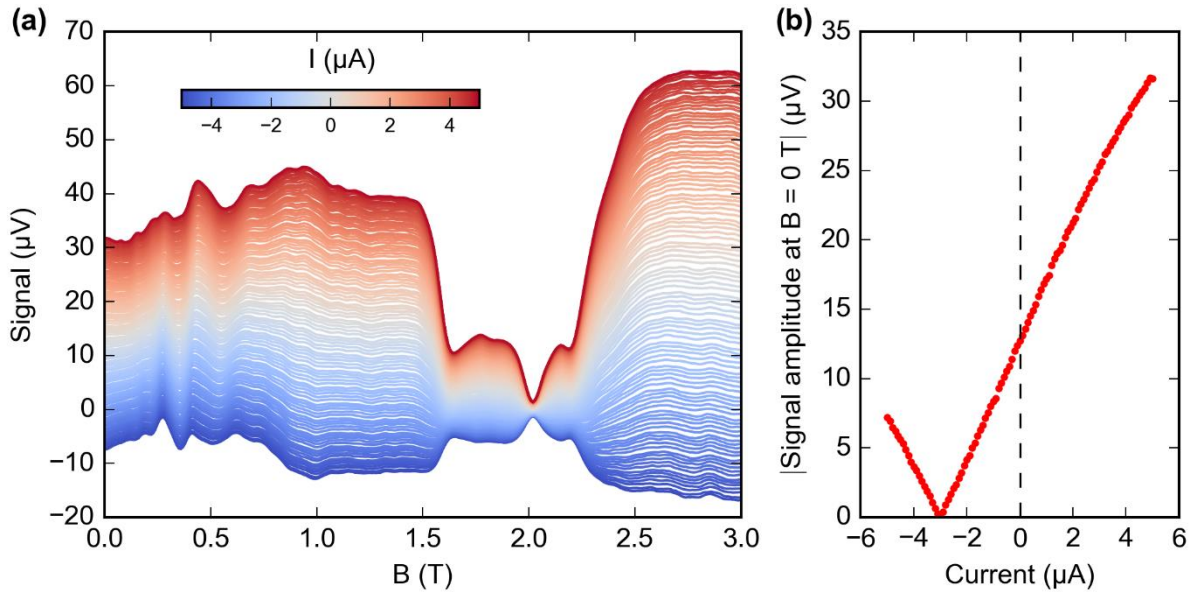


**Figure SM 4:** DC current injection dependence in the  $\Delta U_{\text{DS}}$  (drain-source) configuration. **(a)** Waterfall plot of the photovoltage measured at 56 GHz as a function of magnetic field for different injected currents ranging from  $-5$  to  $5 \mu\text{A}$ . **(b)** Absolute value of the photovoltage signal amplitude at  $B = 0 \text{ T}$  as a function of injected current.

Figure SM 4, presents the absolute value of the signal amplitude at  $B = 0 \text{ T}$  as a function of the injected current. The graph exhibits a V-shape, with the signal reaching  $0 \mu\text{V}$  at  $-3 \mu\text{A}$ , confirming the previously observed offset.

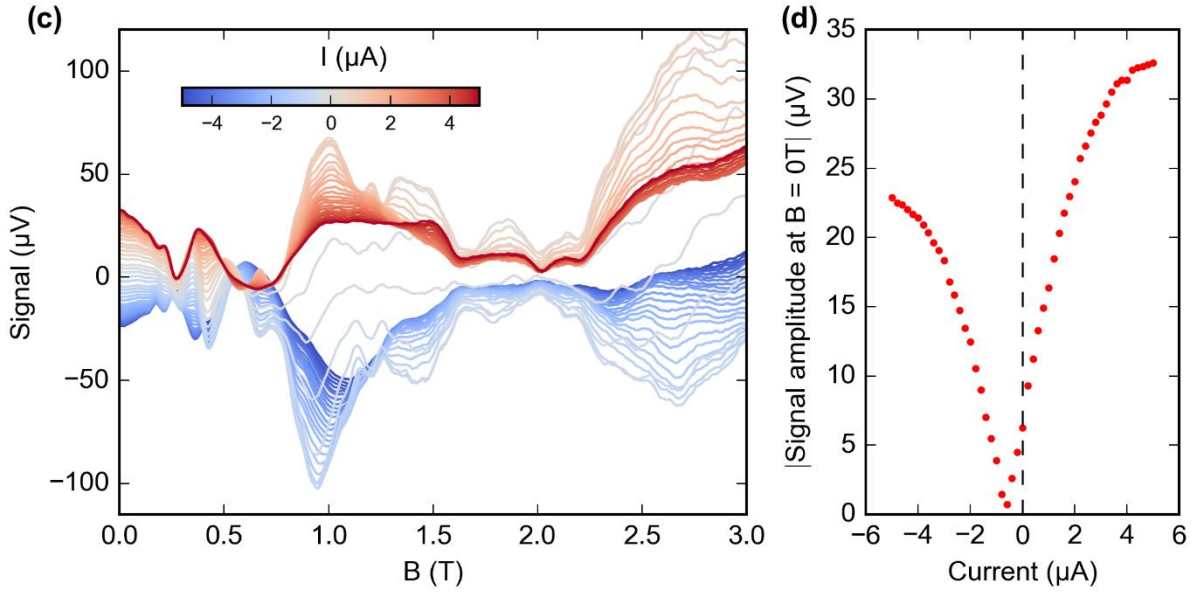


**Figure SM 5:** DC current injection dependence in the  $\Delta U_{\text{SD}}$  (drain-source) configuration. **(a)** Waterfall plot of the photovoltage measured at 56 GHz as a function of magnetic field for different injected currents ranging from -5 to 5  $\mu\text{A}$ . **(b)** Absolute value of the photovoltage signal amplitude at B = 0 T as a function of injected current.

Figure SM 5, shows the absolute value of the signal amplitude at B = 0 T versus injected current for the  $\Delta U_{\text{SD}}$  configuration. We observe a V-shape, but here the signal reaches 0  $\mu\text{V}$  at 0.6  $\mu\text{A}$ , indicating a smaller offset compared to the drain-source configuration.

- Lorentzian fitting and spin relaxation time

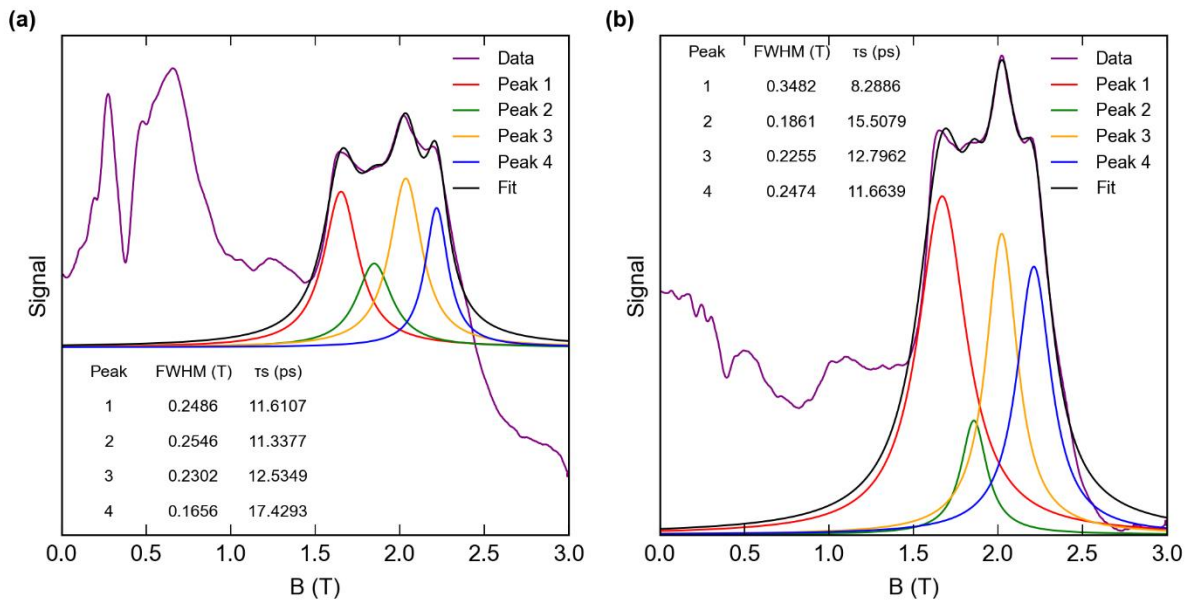


**Figure SM 6:** Lorentzian fitting and spin relaxation time analysis of photovoltage signals in graphene/MoS<sub>2</sub> heterostructures. **(a)** in  $\Delta U_{SD}$  configuration. **(b)**  $\Delta U_{DS}$  configuration. In both panels, purple lines represent the photovoltage data under 100 mW. Colored peaks show individual Lorentzian fit, while the black line indicates the overall fit. Inset tables provide the full width at half maximum (FWHM) and calculated spin relaxation times ( $\tau_s$ ) for each identified peak.

## References

- <sup>1</sup> E. Mönch, S. O. Potashin, et al., Phys. Rev. B 105, 045404 (2022) <https://doi.org/10.1103/PhysRevB.105.045404>
- <sup>2</sup> M. Hild, E. Mönch, L. E. Golub, et al. (2024) <https://arxiv.org/pdf/2407.15597>
- <sup>3</sup> E. Abidi et al., Nanomaterials, vol. 14, no. 4, pp. 1–12, 2024, <https://doi.org/10.3390/nano14040383>
- <sup>4</sup> R. Jago, E. Malic, and F. Wendler, Phys. Rev. B 99, 035419 (2019) <https://doi.org/10.1103/PhysRevB.99.035419>
- <sup>5</sup> M. Ryzhii, V. Ryzhii, M. S. Shur et al., J. Appl. Phys. 134, 084501 (2023) <https://doi.org/10.1063/5.0160899>
- <sup>6</sup> D. A. Bandurin, I. Gayduchenko, Y. Cao, et al., Appl. Phys. Lett. 112, 141101 (2018) <https://doi.org/10.1063/1.5018151>
- <sup>7</sup> L. Viti, A. R. Cadore, X. Yang, et al. Nanophotonics; 10(1): 89–98, (2021) <https://doi.org/10.1515/nanoph-2020-0255>
- <sup>8</sup> M.T. Schlecht, et al. Sci Rep 9, 11205 (2019). <https://doi.org/10.1038/s41598-019-47606-6>
- <sup>9</sup> M. B. Mohd Mokhar et al. AIP Conf. Proc. 2203, 020039 (2020) <https://doi.org/10.1063/1.5142131>
- <sup>10</sup> E. A. Shaner, et al. Appl. Phys. Lett. 90, 181127 (2007) <https://doi.org/10.1063/1.2735943>
- <sup>11</sup> M. Dyakonov and M. S. Shur, Phys. Rev. Lett. 71, 2465 (1993) <https://doi.org/10.1103/PhysRevLett.71.2465>
- <sup>12</sup> M. Dyakonov and M. S. Shur, IEEE Trans. Electron Devices 43, 380 (1996) <https://doi.org/10.1109/16.485650>
- <sup>13</sup> M. I. Dyakonov, Comptes Rendus Physique 11, 7–8, 413–420 (2010) <https://doi.org/10.1016/j.crhy.2010.05.003>
- <sup>14</sup> R. Tauk et al. Applied Physics Letters 89, 25 253511 (2006) <https://doi.org/10.1063/1.2410215>
- <sup>15</sup> W. Knap, F. Teppe, Y. Meziani et al., Appl. Phys. Lett. 85, 675–677 (2004) <https://doi.org/10.1063/1.1775034>
- <sup>16</sup> D. Veksler, F. Teppe, et al. Physical Review B 73, 12 125328 (2006) <https://doi.org/10.1103/PhysRevB.73.125328>
- <sup>17</sup> F. Teppe, W. Knap, D. Veksler, et al. Appl. Phys. Lett. 87, 5, 052107 (2005) <https://doi.org/10.1063/1.2005394>
- <sup>18</sup> F. Teppe, D. Veksler, V. Yu. Kachorovski, et al. Appl. Phys. Lett. 87, 022102 (2005) <https://doi.org/10.1063/1.1952578>
- <sup>19</sup> A. El Fatimy, et al., Appl. Phys. Lett. 89, 13, 131926 (2006) <https://doi.org/10.1063/1.2358816>
- <sup>20</sup> S. Boubanga-Tombet, F. Teppe, et al., Appl. Phys. Lett. 92, 21, 212101 (2008) <https://doi.org/10.1063/1.2936077>
- <sup>21</sup> A. El Fatimy, N. Dyakonova, F. Teppe, et al., Electron Lett 42, 23, 1342–1344, (2006) [10.1049/el:20062452](https://doi.org/10.1049/el:20062452)
- <sup>22</sup> A. M. Kadykov, F. Teppe, C. Consejo, et al., Appl. Phys. Lett. 107, 152101 (2015) <https://doi.org/10.1063/1.4932943>
- <sup>23</sup> A. M. Kadykov, J. Torres, S. S. Krishtopenko, et al., Appl. Phys. Lett. 108, 262102 (2016) <https://doi.org/10.1063/1.4955018>
- <sup>24</sup> S. Ruffenach, A. Kadykov, V. V. Rumyantsev, et al. APL Mater. 5, 035503 (2017) <https://doi.org/10.1063/1.4977781>
- <sup>25</sup> L. Vicarelli, M. S. Vitiello, et al., Nature Materials 11, 865–871 (2012) <https://doi.org/10.1038/nmat3417>
- <sup>26</sup> D.A. Bandurin, D. Svintsov, et al. Nat Commun 9, 5392 (2018) <https://doi.org/10.1038/s41467-018-07848-w>
- <sup>27</sup> J. M. Caridad, O. Castelló, et al., Nano Lett. 2024, 24, 3, 935–942 (2024) <https://doi.org/10.1021/acs.nanolett.3c04300>
- <sup>28</sup> S. D. Ganichev, L. E. Golub, Physica status solidi (b) 251, 9, 1801–1823 (2014) <https://doi.org/10.1002/pssb.201350261>
- <sup>29</sup> S. Candussio, L. E. Golub, et al., Phys. Rev. B 104, 155404 (2021), <https://doi.org/10.1103/PhysRevB.104.155404>
- <sup>30</sup> P.-K. Lu, et al., Nanophotonics 11(11): 2661–2691 (2022) <https://doi.org/10.1515/nanoph-2021-0785>
- <sup>31</sup> B. G. L. Jager, S. Wimmer, A. Lorke, et al. Phys. Rev. B 63, 045315 (2001) <https://doi.org/10.1103/PhysRevB.63.045315>
- <sup>32</sup> D.A. Bandurin, E. Mönch, K. Kapralov, et al. Nat. Phys. 18, 462–467 (2022). <https://doi.org/10.1038/s41567-021-01494-8>
- <sup>33</sup> M.L. Savchenko, Z.D. Kvon, et al., Jetp Lett. 108, 247–252 (2018) <https://doi.org/10.1134/S0021364018160075>
- <sup>34</sup> C. Bray, K. Maussang, C. Consejo, et al. Phys. Rev. B 106, 245141 (2022) <https://doi.org/10.1103/PhysRevB.106.245141>
- <sup>35</sup> M. Gmitra and J. Fabian Phys. Rev. B 92, 155403 (2015) <https://doi.org/10.1103/PhysRevB.92.155403>
- <sup>36</sup> W. Knap et al. Journal of Applied Physics 91, 11 9346 – 9353 (2002) <https://doi.org/10.1063/1.1468257>
- <sup>37</sup> L. Wang, et al. Science 342, 6158 (2013) <https://doi.org/10.1126/science.1244358>
- <sup>38</sup> W. Knap et al., Nanotechnology 24 214002 (2013) <https://doi.org/10.1088/0957-4484/24/21/214002>
- <sup>39</sup> L. Viti, J. Hu, et al., Sci Rep 6, 20474 (2016) <https://doi.org/10.1038/srep20474>
- <sup>40</sup> A. Shabanov et al., Appl. Phys. Lett. 119, 163505 (2021) <https://doi.org/10.1063/5.0063870>
- <sup>41</sup> L. Viti, et al. Efficient Sci Rep 6, 20474 (2016). <https://doi.org/10.1038/srep20474>
- <sup>42</sup> X. Cai, A. B. Sushkov, R. J. Suess, et al., Nature Nanotech 9, 814–819 (2014) <https://doi.org/10.1038/nnano.2014.182>
- <sup>43</sup> F. Ludwig, et al., ACS Applied Electronic Materials, 6(4), 2197–2212 (2024) <https://doi.org/10.1021/acsaem.3c01511>
- <sup>44</sup> T. Low, et al., Phys. Rev. B 90, 081408 (2014). <https://doi.org/10.1103/PhysRevB.90.081408>
- <sup>45</sup> G. Skoblin, J. Sun, A. Yurgens, Sci Rep 7, 15542 (2017) <https://doi.org/10.1038/s41598-017-15857-w>
- <sup>46</sup> A. Harzheim et al., Nano Lett., 18, 7719–7725 (2018) <https://doi.org/10.1021/acs.nanolett.8b03406>
- <sup>47</sup> Y. Anno et al., 2D Mater. 4 025019 (2017), <https://doi.org/10.1088/2053-1583/aa57fc>
- <sup>48</sup> P. Dollfus et al., J. Phys.: Condens. Matter 27, 133204 (2015) <https://doi.org/10.1088/0953-8984/27/13/133204>
- <sup>49</sup> O. Klimenko, Y. Mityagin, H. Videlier, et al. Appl. Phys. Lett. 97, 2, 022111, (2010) <https://doi.org/10.1063/1.3462072>

- 
- <sup>50</sup> S. Boubanga-Tombet et al., J. Phys.: Conf. Ser. 193 012083 (2009) <https://doi.org/10.1088/1742-6596/193/1/012083>
- <sup>51</sup> S. Boubanga-Tombet, M. Sakowicz, et al., Appl. Phys. Lett. 95, 072106 (2009) <https://doi.org/10.1063/1.3207886>
- <sup>52</sup> A.M. Kadykov et al. Appl. Phys. Lett. 107, 152101 (2015); <https://doi.org/10.1063/1.4932943>
- <sup>53</sup> A.M. Kadykov et al. Appl. Phys. Lett. 108, 262102 (2016); <https://doi.org/10.1063/1.4955018>
- <sup>54</sup> A. Avsar, et al. Nat Commun 5, 4875 (2014) <https://doi.org/10.1038/ncomms5875>
- <sup>55</sup> Z. Khatibi and S. R. Power Phys. Rev. B 106, 125417 (2022) <https://doi.org/10.1103/PhysRevB.106.125417>
- <sup>56</sup> C. Bray, K. Maussang, et al., Phys. Rev. B 106, 245141 (2022) <https://doi.org/10.1103/PhysRevB.106.245141>
- <sup>57</sup> R. G. Mani, J. Hankinson, C. Berger & W. A. de Heer, Nat Commun 3, 996 (2012) <https://doi.org/10.1038/ncomms1986>
- <sup>58</sup> J. Sichau, M. Prada, T. Anlauf, et al., Phys. Rev. Lett. 122, 046403 (2019) <https://doi.org/10.1103/PhysRevLett.122.046403>
- <sup>59</sup> U. R. Singh, M. Prada, V. Strenzke, et al., Phys. Rev. B 102, 245134 (2020) <https://doi.org/10.1103/PhysRevB.102.245134>
- <sup>60</sup> E. Morissette et al., Nat. Phys. 19, 1156–1162 (2023) <https://doi.org/10.1038/s41567-023-02060-0>
- <sup>61</sup> L. Tiemann, M. Prada, V. Strenzke, R. H. Blick (2022) <https://doi.org/10.48550/arXiv.2206.14628>
- <sup>62</sup> V. Strenzke, J. M. Meyer, et al., Phys. Rev. B 105, 144303 (2022) <https://doi.org/10.1103/PhysRevB.105.144303>
- <sup>63</sup> T. Naimer, K. Zollner, M. Gmitra, and J. Fabian Phys. Rev. B 104, 195156 (2021); Erratum Phys. Rev. B 108, 039902 (2023) <https://doi.org/10.1103/PhysRevB.104.195156>
- <sup>64</sup> J. J. L. Morton, D. R. McCamey, et al., Nature 479, 345–353 (2011) <https://doi.org/10.1038/nature10681>
- <sup>65</sup> H. Videliier et al., Acta Phys. Pol. 120, 5, 921, (2011) <https://doi.org/10.12693/APhysPolA.120.927>
- <sup>66</sup> D. J. Lepine, Phys. Rev. B 6, 2, 15, 436 (1972) <https://doi.org/10.1103/PhysRevB.6.436>
- <sup>67</sup> I. Solomon, D. Biegelsen, J. Knights, Solid State Commun. 22, 505 (1977) [https://doi.org/10.1016/0038-1098\(77\)91402-8](https://doi.org/10.1016/0038-1098(77)91402-8)
- <sup>68</sup> H. Dersch, L. Schweitzer, and J. Stuke, Phys. Rev. B 28, 4678 (1983) <https://doi.org/10.1103/PhysRevB.28.4678>
- <sup>69</sup> R. A. Street, Philosophical Magazine B, 46, 3, 273-278 (1982) <https://doi.org/10.1080/13642818208246439>
- <sup>70</sup> E. A. Schiff, AIP Conf. Proc. 73, 233–237 (1981) <https://doi.org/10.1063/1.33036>
- <sup>71</sup> D. Kaplan, I. Solomon, N.F. Mott, J. Physique Lett. 39, 51-54 (1978) <https://doi.org/10.1051/jphyslet:0197800390405100>
- <sup>72</sup> M. Datt Bhatt, et al. RSC Adv., 12, 21520-21547 (2022) <https://doi.org/10.1039/D2RA01436J>
- <sup>73</sup> Abid, P. Sehrawat, et al. Sci Rep 8, 3537 (2018). <https://doi.org/10.1038/s41598-018-21686-2>
- <sup>74</sup> S. Dutta, K. Wakabayashi, Sci Rep 5, 11744 (2015) <https://doi.org/10.1038/srep11744>
- <sup>75</sup> P. Ghising Adv. Mater. 35, 2209137 (2023) <https://doi.org/10.1002/adma.202209137>
- <sup>76</sup> B.C. Cavenett and R.F. Brunwin, Solid State Communications, 31, 659-662 (1979) [https://doi.org/10.1016/0038-1098\(79\)90318-1](https://doi.org/10.1016/0038-1098(79)90318-1)
- <sup>77</sup> R. de Sousa, C. Chi Lo, and J. Bokor, Phys. Rev. B 80, 045320 (2009) <https://doi.org/10.1103/PhysRevB.80.045320>
- <sup>78</sup> M. Hild, E. Mönch, L. E. Golub, et al., Phys. Rev. B 110, 125303 (2024) <https://doi.org/10.1103/PhysRevB.110.125303>
- <sup>79</sup> The principles of nuclear magnetism: A. Abragam (Clarendon Press Oxford University Press, London, 1961 xvi–599 p.84 s.) [https://doi.org/10.1016/0029-5582\(61\)90091-8](https://doi.org/10.1016/0029-5582(61)90091-8)
- <sup>80</sup> Electron Paramagnetic Resonance: Elementary Theory and Practical Applications, John A. Weil, James R. Bolton (2006) Copyright © 2007 John Wiley & Sons, Inc. <https://doi.org/10.1002/0470084987>
- <sup>81</sup> D. Veksler, F. Teppe, et al., Phys. Rev. B 73, 125328 (2006) <https://doi.org/10.1103/PhysRevB.73.125328>
- <sup>83</sup> Moczko, Loïc, et al. "Symmetry-dependent dielectric screening of optical phonons in monolayer graphene." arXiv preprint arXiv:2310.13868 (2023). <https://arxiv.org/pdf/2310.13868>